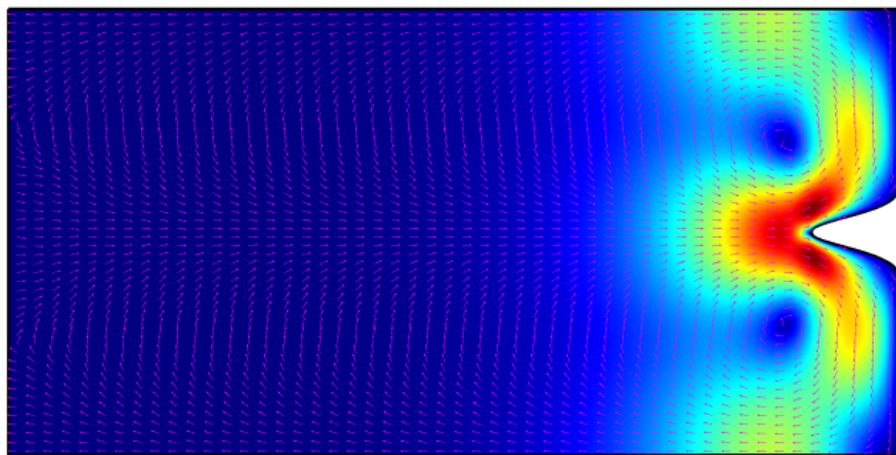DTU

Bachelor Thesis

Modeling of electrokinetics with advection near dendritic metal electrodes

Patrick Strøm-Hansen
s113869

Supervisor: Henrik Bruus

Department of Physics
Technical University of Denmark

19 June 2015

Abstract

In this bachelor thesis we study electrokinetics coupled with advection in a binary electrolytic solution close to perfect representation of a dendrite electrode, when an external voltage is applied. We introduce the governing equations in hydrodynamics and electrokinetics, and establish an understanding of the important concept of the Debye screening layer, through analytical and numerical studies of a highly symmetric setup. The concept of a diffusion limited current is introduced, along with a simple model of the reaction kinetics on the dendrite electrode. A short introduction to the software COMSOL Multiphysics and the finite elements method is carried out, and the implementation is explained for each different setup.

We found that the presence of advection rolls contributed to an overlimiting current in the system and that this contribution had a strong dependency on the physical dimensions of the system. The ionic concentration was also found to play a role on the advection contribution, where no contribution was seen at low concentrations.

The current distribution on the dendrite also changed with the advection rolls, where large current densities were found locally on the tip of the dendrite. We suggest that this effect could influence the dendrite growth and morphology. Ideas of future investigations are presented.

The frontpage figure shows the magnitude of the velocity field (color plot) and direction (arrows) near a Gaussian-shaped dendrite.

Resumé

Vi studerer i dette bachelorprojekt elektrokinetik koblet til advektion i en binær elektrolyt-opløsning i nærheden af en perfekt udgave af en dendritelektrode, når en ydre spænding er påtrykt. Vi introducerer de konstituerende ligninger i hydrodynamik og elektrokinetik, og etablerer en forståelse af det betydningsfulde Debye skærmningslag, gennem analytiske og numeriske studier, af et enkelt setup. Begrebet, diffusions begrænsende strøm bliver introduceret, sammen med en simpel model for reaktionskinetikken på dendritelektroden. Programmet COMSOL Multiphysics og "finite elements" metoden bliver introduceret og implementeringen af hvert numeriske setup er forklaret.

Vi så at tilstedeværelsen af advektionsruller bidrog til en overbegrænsende strøm i systemet og at dette bidrag afhang kraftigt af systemets fysiske dimensioner. Vi så også at ionkoncetrationen spillede en rolle i advektionsbidraget, og at intet bidrag var til stede ved lave koncentrationer.

Strømfordelingen på dendritelektroden ændrede sig også med tilstædeværelsen af advektionsruller, hvor vi registrerede en stor strømtæthed lokalt ved spidsen. Vi indikerer at dette kunne have en indflydelse på dendritvæksten og -morfologien. Ideer til fremtidige undersøgelse er også præsenteret

Preface

This bachelor thesis is submitted in partial fulfilment of the requirement for the Bachelor of Science in Engineering degree (Physics and Nanotechnology) at the Technical University of Denmark (DTU). The work was carried out from February 2015 till June 2015 at the Department of Physics in the Theoretical Microfluidics Group (TMF), headed by Professor Henrik Bruus. This Bachelor thesis counts as 15 ECTS credits.

I want to thank my supervisor Professor Henrik Bruus for the introduction to the field of micro fluidics, and for providing me with a better understanding of physics in general.

I also wish to give thanks to Ph.D. student Christoffer P. Nielsen for his comprehensive explainations and illustrative examples, along with his patience and eagerness to explain.

Finally, I wish to thank my girlfriend Sarah Jørgensen for putting up with me in the late nights, and for her creative and imaginative ideas.

<div align="center">

signature

Patrick Strøm-Hansen
Department of Physics
Technical University of Denmark
19 juni 2015

</div>

Contents

List of Figures

List of symbols

Symbol	Description	Unit
ρ	Mass density	kg m^{-3}
ρ_{el}	Charge density	C m^{-3}
$\boldsymbol{r}$	Position vector	m
$\boldsymbol{v}$	Velocity vector	m s^{-1}
$\tilde{\boldsymbol{J}}$	Mass current density	kg m^{-2} s^{-1}
$\boldsymbol{J}_{\pm}$	Ionic current density	m^{-2} s^{-1}
$c_{\pm}$	Ionic concentration	m^{-3}
c_0	Bulk ionic concentration	J
$D_{\pm}$	Ionic diffusivity	m^2 s^{-1}
$\boldsymbol{\sigma}$	Cauchy stress tensor	N m^{-2}
$\boldsymbol{f}$	Body force density	N m^{-3}
$\boldsymbol{g}$	Gravity	N kg^{-1}
$\boldsymbol{E}$	Electric field	V m^{-1}
p	Pressure	N m^{-2}
$\mu_{\pm}$	Electrochemical potential	J
μ	Dynamic viscosity	kg m^{-1} s^{-1}
T	Temperature	K
λ_{D}	Debye-length	m
V_T	Thermal voltage	V
J_{lim}	Diffusion limited current density	m^{-2} s^{-1}
R	Electrode reaction rate	m^{-2} s^{-1}
$J_{\pm}^{\mathrm{bnd}}$	Electrode current density	m^{-2} s^{-1}
η	Viscosity	Pa s
ϵ	Permittivity of solution	F m^{-1}
$\sigma_{\pm}$	Ionic conductivity	S m^{-1}
σ	Wall charge	C

ζ	Wall potential	V
Ω	Computational domain	
$\partial\Omega$	Domain boundary	
d_{mesh}	Mesh size	
g	Generalized variable	
g_m	Generalized test function	
$C(g)$	Mesh convergence parameter	
α_{mesh}	Bulk mesh element growth rate	
DoF	Number of Degrees of Freedom	
$\boldsymbol{n}$	Surface outward normal vector	
H	Model system height	m
L	Model system length	m
w	Dendrite width	
h	Dendrite amplitude	m
k_0	Reaktion constant	$\mathrm{m}^{-2}\,\mathrm{s}^{-1}$
g	Electrode conductivity	
Re	Reynoldsnumber	
k_{B}	Boltzmann's constant	$1.381 \times 10^{-23}\,\mathrm{J\,K^{-1}}$
e	Elementary charge	$1.602 \times 10^{-19}\,\mathrm{C}$
$|Z|$	Absolute valence number	
ϵ_0	Vacuum permittivity	$8.854 \times 10^{-12}\,\mathrm{F\,m^{-1}}$
$\nabla\cdot$	Divergence operator	
∇	Gradient operator	
$\langle\cdot|\cdot\rangle$	Inner product	
$\mathrm{d}A$	Surface element	
$\mathrm{d}V$	Volume element	
∂_t	Differentiation with respect to time	
∂_x	Differentiation with respect to x-coordinate	
log	Natural logarithm	

Chapter 1

Introduction

Development of effective electrical energy storage systems has become increasingly important to society, in order to store the energy from renewable energy sources, and thereby render fossil fuels superfluous as the primary power supply. Electrochemical energy storage, like conventional batteries, is one way of addressing the problem. In order for batteries to be a serious alternative they have to be reliable, safe and with high energy density. Lead-acid batteries are the most common battery type, but lithium ion batteries show the greatest potential with the increasing demand for power in portable devices [11]. A topic of interest in battery research and development is the formation of dendrites on the electrodes. This occurs when the ionic electrolytic species reduce to a solid on the electrode. The dendrite formation lowers the capacity and over time it can pierce the separator in the cell leading to a short circuit and potentially danger of explosion [12].

The research in dendrite morphology has been conducted since the early nineteen nineties, but to be able to prevent the formation of dendrites or retard the growth, we need to understand the underlying mechanisms more thoroughly, some of which will be investigated in this thesis.

Outline of the thesis

Chapter 2: In this chapter we introduce the governing equation in electrokinetics, hydrodynamics and thermodynamics, that we will use in the rest of the thesis.

Chapter 3: We introduce the software COMSOL Multiphysics which is used to conduct the numerical studies. We also give a brief introduction the the finite elements method.

Chapter 4: We present an analytical solution to a model of an electrolytic solution near a charged surface and compare the results to an approximate solution and a numerical study.

Chapter 5: In this chapter we introduce the diffusion limited current, and present an expression for the reaktion rate at the cathode. We also present the numerical setup used to conduct the numerical experiments, and the governing equations are modified for better

Figure 1.1: Photograph of zinc dendrites formed on a copper electrode. Adopted from Trigueros P. P. *et al.*, *Pattern morphologies in zinc electrodeposition* [10]

results. A mesh convergence analysis is conducted to benchmark the results.

Chapter 6: We present the results obtained from the numerical experiments, and discuss the different effects.

Chapter 7: We discuss the results in relation to other work and suggest what future studies could be interesting to pursue. Along with this we give the concluding remarks.

Chapter 2

Governing equations

In this chapter we present the governing equations that will be used throughout the thesis. This include equations from hydrodynamics, electrostatics, transport theory and thermodynamics.

We work under the continuum hypothesis, where a small volume of the fluid, called a fluid particle, is assigned the average properties of the individual molecules. The introduction of the fluid particle allow us to describe the physical properties of the fluid by fields, and we employ here an Eulerian description, where we consider the average of a fields molecular components, taken over all the particles contained in a volume at a specific position. Examples hereof are the mass density $\rho(\boldsymbol{r}, t)$ and velocity $\boldsymbol{v}(\boldsymbol{r}, t)$,

$$\rho(\boldsymbol{r}, t) \equiv \frac{1}{\Delta \mathcal{V}} \sum_{i \in \Delta \mathcal{V}} m_i, \tag{2.1a}$$

$$\boldsymbol{v}(\boldsymbol{r}, t) \equiv \frac{1}{\rho(\boldsymbol{r}, t) \Delta \mathcal{V}} \sum_{i \in \Delta \mathcal{V}} m_i \boldsymbol{v}_i. \tag{2.1b}$$

Here $i \in \Delta \mathcal{V}$ denotes all the molecules present at time t inside the fixed volume $\Delta \mathcal{V}$ centred around $\boldsymbol{r}$, and the velocity has been defined through the more fundamental quantity, momentum.

In the following the explicit dependence on position and time has been suppressed to make the equations more compact.

2.1 Hydrodynamics

In hydrodynamics we consider the rate of change of mass and momentum. If we consider an arbitrary volume Ω, the total mass inside this volume can change only by a mass flux through the surface of the volume $\partial \Omega$, described by the mass current density $\boldsymbol{J} = \rho \boldsymbol{v}$. This gives rise to the continuity equation

$$\partial_t \rho = -\boldsymbol{\nabla} \cdot (\rho \boldsymbol{v}), \tag{2.2}$$

i.e. the change of mass density in a point in space and time is caused by the convergence of mass current density to that point. In the case where the density is constant, Eq. (2.2) reduces to the continuity equation for incompressible fluids

$$\boldsymbol{\nabla}\!\cdot\!\boldsymbol{v} = 0. \tag{2.3}$$

When deriving the equation of motion for the fluid, we consider the rate of change $\partial_t \boldsymbol{P}$ of the momentum $\boldsymbol{P}$ inside an arbitrary volume Ω, $\partial_t \boldsymbol{P} = \int_\Omega \rho \boldsymbol{v} \mathrm{d}V$. The total momentum inside this volume can, in contrary to mass, change not only by convection, but also through the action of forces given by Newtons second law. This gives rise to the general form of the equation of motion for the Eulerian velocity field of a viscous fluid [1, p. 24],

$$\rho(\partial_t + \boldsymbol{v}\!\cdot\!\boldsymbol{\nabla})\boldsymbol{v} = \boldsymbol{\nabla}\!\cdot\!\boldsymbol{\sigma} + \boldsymbol{f}, \tag{2.4}$$

where $\boldsymbol{f}$ represents the body force densities and $\boldsymbol{\sigma}$ the full stress tensor combining pressure and viscous force densities. The components of the full stress tensor $\boldsymbol{\sigma}$ are:

$$\sigma_{ij} = -p_i\delta_{ij} + \sigma'_{ij} = -p_i\delta_{ij} + \eta(\partial_j v_i + \partial_i v_j) + (\beta - 1)\eta(\partial_k v_k)\delta_{ij}, \tag{2.5}$$

where the dynamic viscosity η, is the internal friction due to shear stress, $\beta = \frac{\zeta}{\eta} + \frac{1}{3}$ is a dimensionless viscosity ratio, and ζ is the internal friction due to compression. When working with Newtonian fluids, the viscosities vary only a little, and hence are taken to be constant. In that case the equation of motion becomes the Navier–Stokes equation.

$$\rho(\partial_t + \boldsymbol{v}\!\cdot\!\boldsymbol{\nabla})\boldsymbol{v} = -\boldsymbol{\nabla}p + \eta\nabla^2\boldsymbol{v} + \beta\eta\boldsymbol{\nabla}(\boldsymbol{\nabla}\!\cdot\!\boldsymbol{v}) + \rho\boldsymbol{g} + \rho_{\mathrm{el}}\boldsymbol{E}, \tag{2.6a}$$

$$\rho(\partial_t + \boldsymbol{v}\!\cdot\!\boldsymbol{\nabla})\boldsymbol{v} = -\boldsymbol{\nabla}p + \eta\nabla^2\boldsymbol{v} + \rho\boldsymbol{g} + \rho_{\mathrm{el}}\boldsymbol{E}, \quad \text{(incompressible fluid)}. \tag{2.6b}$$

In this thesis we will be considering incompressible fluids described by Eq. (2.6b).

Introducing the dimensionless quantities $\tilde{\boldsymbol{r}} = \boldsymbol{r}/L_0$ and $\tilde{\boldsymbol{v}} = \boldsymbol{v}/V_0$, where the tilde denotes a quantity without physical dimension, and L_0 and V_0 are characteristic length and velocity, respectively, for the system. Ignoring body forces, the Navier–Stokes equation can be rewritten on dimensionless form

$$Re[\tilde{\partial}_t + \tilde{\boldsymbol{v}}\!\cdot\!\tilde{\boldsymbol{\nabla}}]\tilde{\boldsymbol{v}} = -\tilde{\boldsymbol{\nabla}}\tilde{p} + \tilde{\nabla}^2\tilde{\boldsymbol{v}}, \tag{2.7}$$

by introducing the dimensionless Reynolds number Re:

$$Re \equiv \frac{\rho L_0 V_0}{\eta}. \tag{2.8}$$

It can thus be determined which terms in Eq. (2.7) are the dominant for different Reynolds numbers. For small Reynolds numbers $Re \ll 1$ the viscous term $\tilde{\nabla}^2\tilde{\boldsymbol{v}}$ dominates, whereas for large Reynolds numbers $Re \gg 1$ the inertial term $(\tilde{\boldsymbol{v}}\!\cdot\!\tilde{\boldsymbol{\nabla}})\tilde{\boldsymbol{v}}$ is the dominant[1, p. 24f].

2.2 Electrostatics

In this thesis we are concerning ourselves with a system consisting of an electrolyte subjected to an electrical potential. It is therefore natural to couple the electrical forces to the equation of motion, through the electrical body force density $\boldsymbol{f}_{\text{el}} = \rho_{\text{el}}\boldsymbol{E}$.

As discussed in the beginning of this chapter, we are working under the continuum hypothesis hence the governing equations are the Maxwell equations for continuous media, with no magnetic fields since the problem is static.

$$\boldsymbol{\nabla} \times \boldsymbol{E} = 0, \tag{2.9a}$$

$$\boldsymbol{\nabla} \cdot \boldsymbol{D} = \boldsymbol{\nabla} \cdot (\epsilon \boldsymbol{E}) = \rho_{\text{el}}, \tag{2.9b}$$

$$\boldsymbol{D} = \epsilon_0 \boldsymbol{E} + \boldsymbol{P} = \epsilon \boldsymbol{E}, \tag{2.9c}$$

$$\boldsymbol{J}_{\text{el}} = \sigma_{\text{el}}\boldsymbol{E}. \tag{2.9d}$$

Eq. (2.9c) is true for linear isotropic materials, and water solutions with low concentrations of solute can be treated that way, with a dielectric constant of $\epsilon \approx 78$. Since there is no rotation of the electric field, it can be written as the gradient of a scalar potential ϕ

$$\boldsymbol{E} = -\boldsymbol{\nabla}\phi. \tag{2.10}$$

Combing Eqs. (2.9b) and (2.10), we end up with the Poisson equation for the relation between electric potential and charge,

$$\nabla^2\phi = -\frac{\rho_{\text{el}}}{\epsilon}. \tag{2.11}$$

2.3 Thermodynamics

It is well known that the ions in a weak electrolytic solution can be modelled as non-interacting particles [1]. The energy of the particles can thus be described by the chemical potential $\mu_\pm$ of an ideal gas of ions with concentration $c_\pm$,

$$\mu_\pm = \mu_{0,\pm} + k_{\text{B}}T \log\left(\frac{c_\pm}{c_0}\right), \tag{2.12}$$

where $\mu_{0,\pm}$ is some reference chemical potential of the solute, $c_\pm$ is the concentration of the positive and negative ions respectively, and c_0 is the reservoir concentration of both ionic species. Since the electrolytic solution under consideration is subjected to an electric potential another contribution to the chemical potential must be added. In the electric field each ion gain the energy $\pm|Z|e\phi$. Adding the contribution to Eq. (2.12) we end up with the electrochemical potential $\mu_\pm$,

$$\mu_\pm = \mu_{0,\pm} + k_{\text{B}}T \log\left(\frac{c_\pm}{c_0}\right) \pm |Z|e\phi. \tag{2.13}$$

In the absence of advection the electrochemical potential will reach a thermal equilibrium where $\boldsymbol{\nabla}\mu_\pm = 0$.

2.4   Ionic transport

In the absence of reactions, the number of particles is conserved, just like the mass and momentum. We can thus write a conservation equation for the number of particles as well:

$$\partial_t c_\pm = -\boldsymbol{\nabla}\cdot\boldsymbol{J}_\pm, \tag{2.14}$$

where $c_\pm$ denotes the concentration and $\boldsymbol{J}_\pm$ the particle current density of the two ionic species under consideration. The subscript $\pm$ denotes the sign of charge of the ions.

The contributions to the current density stems from diffusion, advection and electromigration, and since we are working with weak solutions it is customary to use the particle current density instead of the mass current density [1, p. 94]. In the following, tilde denotes mass current densities and electric current density.

$$\boldsymbol{J}_\pm = \boldsymbol{J}_\pm^{\mathrm{adv}} + \boldsymbol{J}_\pm^{\mathrm{diff}} + \boldsymbol{J}_\pm^{\mathrm{el}}. \tag{2.15}$$

The advection contribution is just the mass current density of ionic species due to advection divided by the mass of a single ion

$$\boldsymbol{J}_\pm^{\mathrm{adv}} = \frac{\tilde{\boldsymbol{J}}_\pm^{\mathrm{adv}}}{m_\pm} = c_\pm \boldsymbol{v}. \tag{2.16}$$

The diffusion contribution is due to concentration gradients in the solution, and is described here by Fick's law for weak solutions,

$$\boldsymbol{J}_\pm^{\mathrm{diff}} = \frac{\tilde{\boldsymbol{J}}_\pm^{\mathrm{diff}}}{m_\pm} = -D_\pm \boldsymbol{\nabla} c_\pm, \tag{2.17}$$

where $D_\pm$ denotes the diffusivity of the ionic species.

The electro migrative contribution stems from Eq. (2.9d), where the electric current density is rewritten as a particle current density,

$$\boldsymbol{J}_\pm^{\mathrm{el}} = \frac{\tilde{\boldsymbol{J}}_\pm^{\mathrm{el}}}{|Z|e} = \mp\frac{\sigma_\pm^{\mathrm{el}}}{|Z|e}\boldsymbol{\nabla}\phi. \tag{2.18}$$

Here $|Z|$ denotes the valence number of the ions. We want to write the electromigrative contribution in terms of concentration since this is the field variable of interest. We therefore use that the electric conductivity is related to the concentration and mobility by $\sigma_\pm = |Z|e c_\pm \mu_\pm$, and using the Einstein relation $D_\pm = \mu_\pm k_{\mathrm{B}} T$ we now write,

$$\boldsymbol{J}_\pm^{\mathrm{el}} = \mp c_\pm \frac{D_\pm}{V_T}\boldsymbol{\nabla}\phi, \tag{2.19}$$

where we have introduced a thermal velocity as $V_T = \frac{k_{\mathrm{B}} T}{|Z|e}$.

By combining the different contributions we end up with the so-called Nernst–Planck equation for the particle current density [1, p. 157],

$$\boldsymbol{J}_{\pm} = c_{\pm}\boldsymbol{v} - D_{\pm}\boldsymbol{\nabla}c_{\pm} \mp c_{\pm}\frac{D_{\pm}}{V_T}\boldsymbol{\nabla}\phi. \tag{2.20}$$

Recognising the contributions from the concentration gradients and the electrical potential gradient we write the Nernst–Planck equation in terms of the electro-chemical potential,

$$\boldsymbol{J}_{\pm} = c_{\pm}\boldsymbol{v} - \frac{c_{\pm}D_{\pm}}{k_\mathrm{B}T}\boldsymbol{\nabla}\mu_{\pm} \tag{2.21}$$

In this thesis we only work in the steady state of Eq. (2.14) i.e.

$$0 = \boldsymbol{\nabla}\cdot\boldsymbol{J}_{\pm} \tag{2.22}$$

2.5   Non-linearities

This concludes the governing equations that will be used in the thesis, and even though the equations are not inherently non-linear in the limits we will consider, (low Reynolds-numbers), the coupling between them gives rise to non-linear effects. The number of setups in which the coupled equations can be solved analytically are limited, and numerical experiments are therefore a necessity.

Chapter 3

COMSOL Multiphysics

All modelling in this thesis has been carried out using the software COMSOL Multiphysics, which is a software used for solving partial differential equations, based on the finite elements method. In this chapter we will briefly introduce the finite elements method, and COMSOL multiphysics in general.

3.1 The finite elements method

The governing equations in this thesis, as in most problems, are coupled non-linear differential equations. In most cases no analytical solutions exist to the problems, apart from highly symmetric set-ups. To be able to find an approximate solution, we need to discretize the problem and this is done be expanding it in a set of localized basis functions. The basis functions, in COMSOL called test function, vary between 1 on their own node and 0 on surrounding nodes in some polynomial way depending on the problem, and in this way they form a grid computational domain covering the domain of interest.

We consider a general case of a boundary value problem, for the dependent variable $g(\boldsymbol{r})$ and the PDE,

$$\mathcal{L}\{g(\boldsymbol{r}))\} = F(\boldsymbol{r}), \tag{3.1}$$

where $\mathcal{L}$ is a differential operator and $F(\boldsymbol{r})$ a forcing term. In the rest of the chapter, as in the previous, we will suppress the explicit dependence on position. A solution g to Eq. (3.1) is called a strong solution, but to solve the problem approximately, we relax the demands on the solution by introducing the defect,

$$d \equiv \mathcal{L}\{g\} - F. \tag{3.2}$$

We expand now the dependent variable in a set of test functions $\{\hat{g}_n\}$, that forms a basis on the function space,

$$g = \sum_n c_n \hat{g}_n, \tag{3.3}$$

where c_n are expansion coefficients. Instead of requiring d in Eq. (3.2) to be zero, and ending up with Eq. (3.1), we require that the projection of the defect on to the test functions is zero,

$$\langle \hat{g}_m | d \rangle = 0, \tag{3.4}$$

giving a softer constraint on the solution. The inner product is defined as $\langle a|b \rangle = \int_\Omega ab\, dV$, and this formulation of the problem is called weak form. If we insert the defect into Eq. (3.4), and exploit that $\mathcal{L}$ in this is linear we get,

$$\langle \hat{g}_m | \mathcal{L} \sum_n c_n \hat{g}_n \rangle = \langle \hat{g}_m | F \rangle, \tag{3.5a}$$

$$\sum_n c_n \langle \hat{g}_m | \mathcal{L} \hat{g}_n \rangle = \langle \hat{g}_m | F \rangle. \tag{3.5b}$$

This formulation of the weak form is seen to have the shape of a matrix problem,

$$\mathbf{Kc} = \mathbf{f}, \tag{3.6}$$

where $\mathbf{K}$ is called the stiffness matrix and has the elements $K_{mn} = \langle \hat{g}_m | \mathcal{L} \hat{g}_n \rangle$, and the solution to the weak form problem, in the case where $\mathcal{L}$ is linear, is thus a matter of solving the matrix equation Eq. (3.6) for the coefficient vector $\mathbf{c}$.
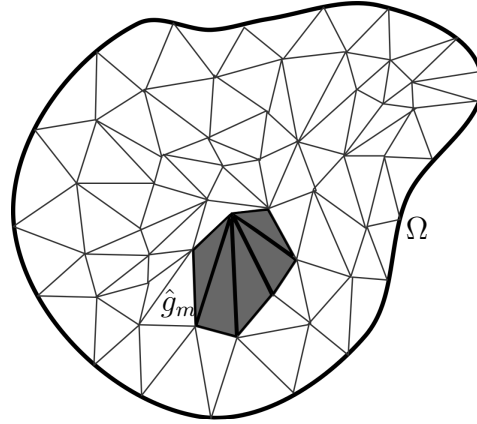

Figure 3.1: Sketch of the triangular mesh on a 2D domain Ω, showing the generalized test function $\hat{g}_m$.

3.1.1   Implementing boundary conditions

When solving differential equations, the solution depend on the boundary or initial conditions of the problem, it is therefore advantageous to implement the boundary conditions explicitly in the formulation of the weak form. This is done by rewriting Eq. (3.1) in the form of a continuity equation,

$$\boldsymbol{\nabla} \cdot \boldsymbol{\Gamma} = F. \tag{3.7}$$

By inserting Eq. (3.7), formulated as the defect, into Eq. (3.4) we obtain,

$$\langle \hat{g}_m | \boldsymbol{\nabla} \cdot \boldsymbol{\Gamma} - F \rangle = \int_\Omega [\hat{g}_m \boldsymbol{\nabla} \cdot \boldsymbol{\Gamma} - \hat{g}_m F]\, \mathrm{d}V = 0, \tag{3.8}$$

and applying the product rule for differentiation along with Gauss' divergence theorem we can split the integral into a bulk and a boundary part,

$$\int_\Omega [\boldsymbol{\nabla} \cdot \{\hat{g}_m \boldsymbol{\Gamma}\} - \boldsymbol{\nabla} \hat{g}_m \cdot \boldsymbol{\Gamma} - \hat{g}_m F]\, \mathrm{d}V = 0, \tag{3.9a}$$

$$\int_{\partial\Omega} \hat{g}_m \mathbf{n} \cdot \boldsymbol{\Gamma}\, \mathrm{d}A + \int_\Omega [-\boldsymbol{\nabla} \hat{g}_m \cdot \boldsymbol{\Gamma} - \hat{g}_m F]\, \mathrm{d}V = 0. \tag{3.9b}$$

It is now possible to include the boundary conditions, and in the case of Neumann conditions we simply substitute $\mathbf{n} \cdot \boldsymbol{\Gamma}$ with the condition. In the case where we want to implement Dirichlet boundary conditions we have to impose a constraint on the system as a function of the dependent variable and it takes the form,

$$R(g) = 0. \tag{3.10}$$

This constraint enters into Eq. (3.7) as a constraint-force in COMSOL.

3.2   Mesh analysis

The solution to the problem in Eq. (3.4) depends on how well we can represent our dependent variables in terms of the test functions. The test functions form a mesh on the computational domain, and when choosing the mesh element size it is a tradeoff between precision and computation time. A sketch of the mesh on a 2D-domain is shown in figure Fig. 3.1. We will conduct a mesh convergence analysis, to verify that our results are not merely numerical artefacts but indeed physical behaviour. For the different field variables we calculate,

$$C(g) = \sqrt{\frac{\int (g - g_{\mathrm{ref}})^2 \mathrm{d}x \mathrm{d}y}{\int (g_{\mathrm{ref}})^2 \mathrm{d}x \mathrm{d}y}}, \tag{3.11}$$

where g is a dependent variable of the problem, calculated for different mesh element sizes, and g_{ref} is a reference solution calculated with an extremely fine mesh[3].

3.3   Working with COMSOL

COMSOL multiphysics is a GUI based FEM solver, that is often used as a black box for solving a variety of problems. A lot of physics is implemented in the program in modules that can be chosen for a specific problem. We have used the weak form PDE module, in the mathematics category, instead of one of the predefined physics modules, to be able to control the variables and equations.

In the GUI we build the problem graphically, and this is an appealing approach in terms of visualization. The equations governing the physics are then implemented, and assigned to the parts of the system were they apply.

When all of the equations and boundary conditions are implemented, the problems can be solved using one of the build in FEM solvers. The data is stored in datasets, and the processing can be done internally in COMSOl or in another software. For most of the data processing we used the software Matlab, which has an interpreter for COMSOL. A lot of the challenges in the data handling was due to this interpreter, which was not able to handle the different data structures that COMSOL could produce. For future numerical experiments we recommend using the build in functions in COMSOL for data processing and then export the evaluated data, as data files.

Chapter 4

Charged Wall

In this chapter we present an analytical solution to a simple set-up, comprised of an infinite negatively charged wall occupying the yz-plane, and an electrolytic solution occupying the positive half-plane in the x-direction, Fig. 4.1. The analytical solution will be compared to the full numerical simulation, carried out with COMSOL as described in Chapter 3.

The actual problem we are interested in is much more complicated than this, but it is important to study this simple example to gain insight in the nature of electrokinetics and constitute some important concepts that will be used in the rest of the thesis. The
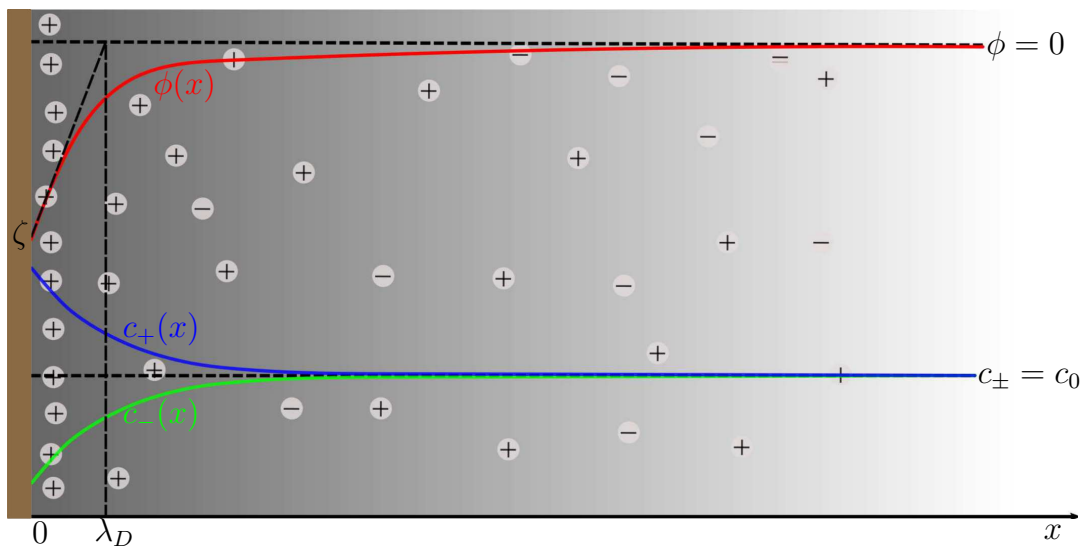

Figure 4.1: 1D-sketch of an electrolytic solution near a negatively charged wall at fixed electric potential $\zeta < 0$. In red the electric potential $\phi(x)$, reaching zero in the bulk. In blue and green the concentrations of cations and anions respectively $c_\pm(x)$, reaching charge neutrality in the bulk. Light grey circles represent cations and anions.

general problem will be formulated in 3D, but the possible solutions are in one dimension,

as sketched in Fig. 4.1.

If a charged solid comes into contact with an electrolytic solution, the co-ions will be repelled from the solid and the counter-ions attracted and form a layer that screens the surface charges. The ions will rearrange until they reach thermal equilibrium where the electrochemical potential, as introduced in Eq. (2.13), is constant $\mu_\pm = \text{const}$. The gradient of the electrochemical potential is thus zero $\boldsymbol{\nabla}\mu_\pm = 0$, leading to the equation,

$$k_{\mathrm{B}}T\boldsymbol{\nabla}\log\left(\frac{c_\pm(\boldsymbol{r})}{c_0}\right) = \mp|Z|e\boldsymbol{\nabla}\phi(\boldsymbol{r}). \tag{4.1}$$

The potential drops of from a fixed potential ζ on the wall, to zero in the bulk, and we assume that the ionic concentrations reach a neutral concentration c_0 in the bulk. This leads to the conditions,

$$\phi(0) = \zeta, \quad \phi(\infty) = 0, \quad c_\pm(\infty) = c_0. \tag{4.2}$$

Subjected to these boundary conditions Eq. (4.1) can be integrated, leading to a Boltzmann distribution of the ions,

$$c_\pm(\boldsymbol{r}) = c_0\exp\left(\mp\frac{\phi(\boldsymbol{r})}{V_T}\right). \tag{4.3}$$

Here V_T is the thermal voltage as introduced in Eq. (2.19) which, for an electrolyte with valence $Z = 1$, under normal conditions ($T = 25^\circ\text{C}$) takes the value $V_T = 25.7\,\text{mV}$. To reduce the equation to one dependent variable, namely the potential, we insert the expression for $c_\pm(\boldsymbol{r})$ into the Poisson equation, Eq. (2.11), leading to the Poisson–Boltzmann equation for the electical potential,

$$\nabla^2\phi(\boldsymbol{r}) = -\frac{\rho_{\mathrm{el}}}{\epsilon} = \frac{|Z|e}{\epsilon}[c_+(\boldsymbol{r}) - c_-(\boldsymbol{r})] = 2\frac{|Z|ec_0}{\epsilon}\sinh\left[\frac{\phi(\boldsymbol{r})}{V_T}\right] = \frac{V_T}{\lambda_{\mathrm{D}}^2}\sinh\left[\frac{\phi(\boldsymbol{r})}{V_T}\right]. \tag{4.4}$$

We have introduced the Debye-length $\lambda_{\mathrm{D}} = \sqrt{\dfrac{\epsilon k_{\mathrm{B}}T}{2(|Z|e)^2c_0}}$, which is a characteristic length scale for this kind of system.

There are different approaches to solving the Poisson–Boltzmann equation, either numerically or in some cases analytically. In the following we derive an analytical solution, known as the Gouy–Chapman solution. This solution will be compared to numerical results and an approximate solution in the case of low ζ-potentials.

4.1   The Gouy–Chapman solution

In the case where Eq. (4.4) applies to a system with a charged wall in the yz-plane and an electrolyte occupying the positive half-space $x > 0$, as illustrated in Fig. 4.1, the problem can be solved analytically. Due to the translational symmetry, the potential $\phi(x)$ only vary in the x direction and the Poisson–Boltzmann equation reads,

$$\partial_x^2 \phi(x) = \frac{V_T}{\lambda_{\mathrm{D}}^2} \sinh \left[\frac{\phi(x)}{V_T} \right]. \tag{4.5}$$

It is easier to keep track of the problem in dimensionless form and by introducing the dimensionless variables $\tilde{\phi} = \phi/V_T$ and $\tilde{x} = x/\lambda_{\mathrm{D}}$, we can rewrite the equation on dimensionless form,

$$\partial_{\tilde{x}}^2 \tilde{\phi}(\tilde{x}) = \sinh \left[\tilde{\phi}(\tilde{x}) \right]. \tag{4.6}$$

Multiplying both sides by $\partial_{\tilde{x}} \tilde{\phi}$ and using the chain rule we may rewrite the equation as,

$$\partial_{\tilde{x}} \left[\frac{1}{2} (\partial_{\tilde{x}} \tilde{\phi}(\tilde{x}))^2 \right] = \partial_{\tilde{x}} \left[\cosh \left[\tilde{\phi}(\tilde{x}) \right] \right]. \tag{4.7}$$

This equation can be integrated using the boundary conditions $\tilde{\phi}(\infty) = \partial_{\tilde{x}} \tilde{\phi}(\infty) = 0$,

$$\partial_{\tilde{x}} \tilde{\phi}(\tilde{x}) = \sqrt{2 \cosh \left[\tilde{\phi}(\tilde{x}) \right] - 2} = -2 \sinh \left[\frac{\tilde{\phi}(\tilde{x})}{2} \right]^1. \tag{4.8}$$

Substituting the a change of variable $\tilde{v} = \tilde{\phi}/2$, and separating the variables $\tilde{v}$ and $\tilde{x}$ we get an expression that we can integrate[2],

$$\int_{\frac{\tilde{\zeta}}{2}}^{\tilde{v}(\tilde{x})} \frac{\mathrm{d}\tilde{v}}{\sinh[\tilde{v}]} = -\int_0^{\tilde{x}} \mathrm{d}\tilde{x} \;\Rightarrow\; \log \left(\frac{\tanh \left[\frac{\tilde{v}(\tilde{x})}{2} \right]}{\tanh \left[\frac{\tilde{\zeta}}{4} \right]} \right) = -\tilde{x}, \tag{4.9}$$

where the boundary condition $\tilde{v}(0) = \tilde{\phi}(0)/2 = \tilde{\zeta}/2$ and the potential $\tilde{\zeta}$ is normalized by V_T. Rearranging the terms and adding dimensions to the quantity we have found the Gouy-Chapman solution for the potential,

$$\phi(x) = 4V_T \operatorname{arctanh} \left(\tanh \left[\frac{\zeta}{4V_T} \right] \exp \left[-\frac{x}{\lambda_{\mathrm{D}}} \right] \right). \tag{4.10}$$

In many practical applications the ζ-potential stems from a surface charge density, e.g. on a wall. The surface charge density σ relates to the ζ-potential through,

$$\sigma = \frac{2\epsilon V_T}{\lambda_{\mathrm{D}}} \sinh \left[\frac{\zeta}{2V_T} \right]. \tag{4.11}$$

4.2 Debye–Hückel Approximation

In the special case outlined in the previous section, we were able to solve the problem analytically, but to gain some physical insight it is useful to find an approximative solution to the Poission–Boltzmann equation. If the potential on the charged surface is sufficiently small $\zeta \ll V_T$, we can expand the right hand side of Eq. (4.4),

---

[1] $\cosh[u] = 2 \sinh^2 \left[\frac{u}{2} \right]$
[2] $\int \frac{\mathrm{d}u}{\sinh[u]} = \log \left[\tanh[u/2] \right] + \text{const}$

$$\nabla^2 \phi(\boldsymbol{r}) = \frac{1}{\lambda_{\mathrm{D}}^2} \phi(\boldsymbol{r}), \tag{4.12}$$

and this equation has analytical solutions in more configurations than the original equation.

To be able to compare the approximate solution with the Gouy-Chapman solution we solve Eq. (4.12), for the same system as in Section 4.1,

$$\partial_x^2 \phi(x) = \frac{1}{\lambda_{\mathrm{D}}^2} \phi(x). \tag{4.13}$$

Subjected to the boundary conditions given in Eq. (4.2) this has the solution,

$$\phi(x) = \zeta \exp\left[-\frac{x}{\lambda_{\mathrm{D}}} \right]. \tag{4.14}$$

4.3   Numerical solution

The numerical set-up in COMSOL, follows the implementation mentioned in Section 3.1.1. The numerical solution will be compared to the Gouy–Chapman solution and the Debye–Hückel approximation.

4.3.1   Electrical potential

The Poisson equation can by written in terms of a continuity equation $\boldsymbol{\nabla}(-\epsilon\boldsymbol{\nabla}\phi(\boldsymbol{r})) = \rho_{\mathrm{el}}(\boldsymbol{r}) = |Z|e(c_+(\boldsymbol{r}) - c_-(\boldsymbol{r}))$, and it takes the weak form,

$$\int_{\partial\Omega} \hat{\phi}_m \boldsymbol{n}\cdot(-\epsilon\boldsymbol{\nabla}\phi(\boldsymbol{r}))\mathrm{d}A + \int_{\Omega} \big[-\boldsymbol{\nabla}\hat{\phi}_m\cdot(-\epsilon\boldsymbol{\nabla}\phi(\boldsymbol{r})) - \hat{\phi}_m\rho_{\mathrm{el}}(\boldsymbol{r}) \big]\mathrm{d}\boldsymbol{r} = 0, \tag{4.15}$$

where $\hat{\phi}_m$ is the electrical potential test function and $\boldsymbol{n}$ is the boundary normal vector, which is defined as pointing away from the interior of the domain[13]. The weak boundary term is implemented as,

$$\boldsymbol{n}\cdot(-\epsilon\boldsymbol{\nabla}\phi(\boldsymbol{r})) = -\sigma, \quad \boldsymbol{r} \in \{\partial\Omega_1\} \tag{4.16}$$

where the boundaries correspond to the sketch in Fig. 4.2. The minus sign stems from the direction of the normal vector. On the right, wall $\partial\Omega_2$ we set $\sigma = 0$ and on the left wall $\partial\Omega_1$, σ relates to ζ through Eq. (4.11).

4.3.2   Ionic current densities

As described in Section 2.4 we are interested in the steady state current densities $0 = \boldsymbol{\nabla}\cdot\boldsymbol{J}_\pm$, and using the ionic concentrations as the field variable we can write the weak form of Eq. (2.22),
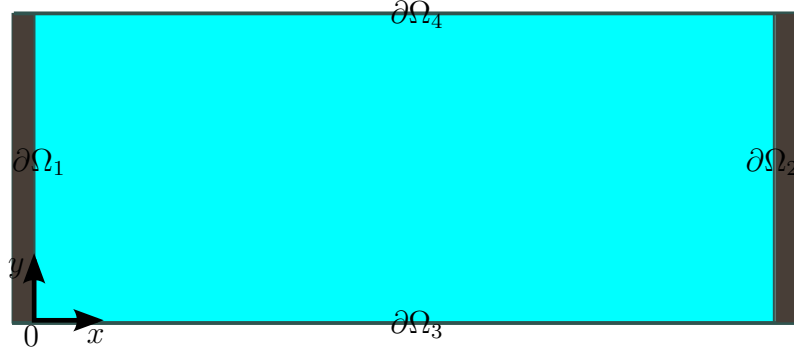
Figure 4.2: Sketch of geometry for the numerical simulations of electrolytic solution near a charged surface in the absence of advection.

$$\int_{\partial\Omega} \hat{c}_{\pm,m} \boldsymbol{n}\cdot\boldsymbol{J}_{\pm}(\boldsymbol{r})\mathrm{d}A + \int_{\Omega} -\boldsymbol{\nabla}\hat{c}_{\pm,m}\cdot\boldsymbol{J}_{\pm}(\boldsymbol{r})\mathrm{d}V. \tag{4.17}$$

On the walls $\partial\Omega_3$ and $\partial\Omega_4$, no flux is allowed and we implement the weak contribution as,

$$\boldsymbol{n}\cdot\boldsymbol{J}_{\pm}(\boldsymbol{r}) = 0, \quad \boldsymbol{r} \in \{\partial\Omega_3, \partial\Omega_4\}. \tag{4.18}$$

The same boundaries act as a reservoir of ions which is implemented as,

$$c_{\pm}(\boldsymbol{r}) = c_0, \quad \boldsymbol{r} \in \{\partial\Omega_3, \partial\Omega_4\}. \tag{4.19}$$

We note that the constraint on the concentrations, forces the system to respond in an non-physical way at the intersections between the boundaries $\partial\Omega_1$, $\partial\Omega_3$ and $\partial\Omega_4$, but the numerical solution stabilizes over the characteristic length, defined by the Debye-length, and the results shown in Fig. 4.3 are thus obtained from the middle of boundary $\partial\Omega_1$.

We see that the numerical results are in perfect agreement with the Gouy–Chapman solution and that for $\zeta \gg V_T$ the Debye–Hückel approximation breaks down. The parameter values used to obtain the results were $c_0 = 1\mathrm{mM}$, $\epsilon = 78\epsilon_w$ and $T = 300\mathrm{K}$.
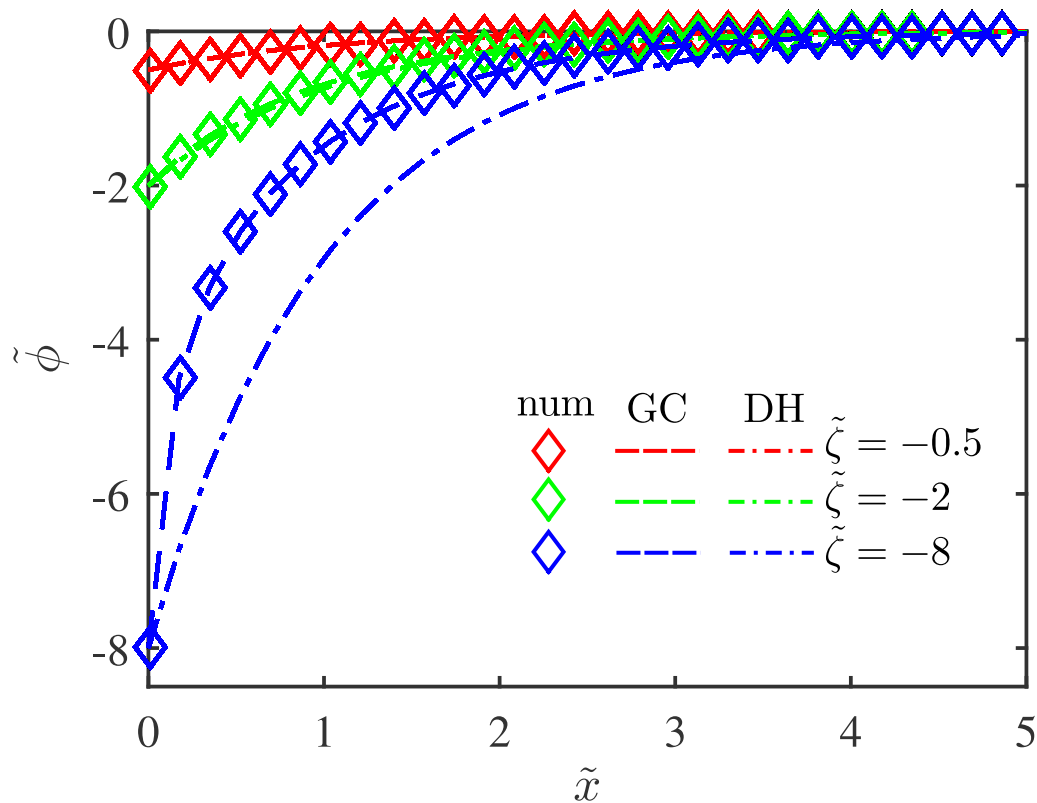
Figure 4.3: Results from numerical simulations compared to the Gouy–Chapman solution (GC) and the Debye–Hückel approximation (DH). The electric potential and the ζ-potential are normalized by V_T and the coordinate x is normalized by the Debye-length λ_D

Chapter 5

Current density with advection near dendrite electrode

We present here the setup of the model from which the results in the next chapter are obtained. Inspired by existing work on metal dendrite morphology[5], the model setup proposed here is thought of as an ideal representation of an early state in the growth of dendrite structures, from an aqueous solution of copper-sulphate onto a copper electrode. In Fig. 5.1, a SEM picture of the early growth state of a copper-dendrite is seen.

Experiments shows that electrocenvective rolls form around the tip of dendrite branches[6], but the theory proposed for the velocity of these, does not agree with experiments[7], which still makes the area interesting to research. We will investigate how the advection rolls around the dendrite tips contribute to the ionic current density in the system, both the maximum current density as well as the current distribution on the dendrite.

When studying electrokinetic phenomena two views can be applied when describing the forces driving the ionic transport. It can be viewed as a result of diffusive and electric forces or as a result of gradients in the electrochemical potential[4]. When studying effects near an electrode the latter is useful, because the electrochemical

Figure 5.1: SEM photograph of dendrite growth on a copper electrode. Adopted from Devos *et al. Growth of electrolytic copper dendrites. I: Current transients and optical observations*[5].

potential of the counterions is nearly constant across the screening layer. In the numerical study it also proved useful to change the variable in the Nernst–Planck equation, Eq. (2.20), from $c_{\pm} \rightarrow \log \tilde{c}_{\pm}$, because of the numerical problem of substracting large numbers, which could result in negative concentrations.
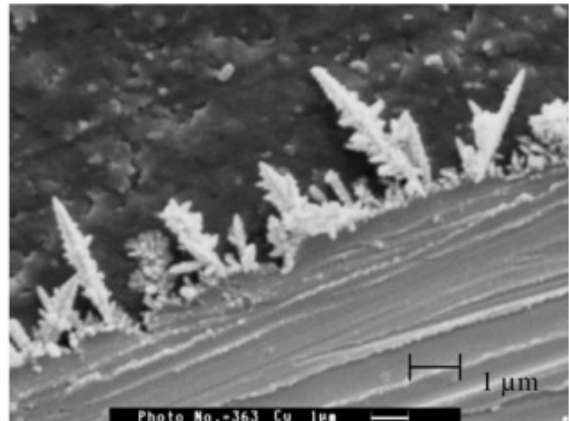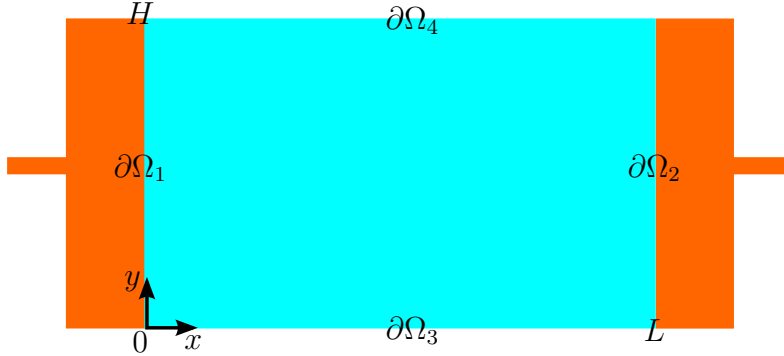
Figure 5.2: Sketch of a geometry with a flat electrode

In the Navier–Stokes equation, the bodyforce density, $\boldsymbol{f}$, is here the electrostatic force $\boldsymbol{f}_{\mathrm{el}} = -\rho_{\mathrm{el}}\boldsymbol{\nabla}\phi = -|Z|e(c_+ - c_-)\boldsymbol{\nabla}\phi$, but we can write this in terms of the gradient of the electrochemical potential instead,

$$\boldsymbol{f} = -c_+\boldsymbol{\nabla}\mu_+ - c_-\boldsymbol{\nabla}\mu_- + \boldsymbol{\nabla}(c_+ + c_-), \tag{5.1}$$

where the last term stems from the electrochemical potential of water, and can be recognized as the osmotic pressure. With this definition of the force density the Navier–Stokes equation becomes,

$$\rho(\partial_t + \boldsymbol{v}\cdot\boldsymbol{\nabla})\boldsymbol{v} = -\boldsymbol{\nabla}p' + \eta\nabla^2\boldsymbol{v} - (c_+\boldsymbol{\nabla}\mu_+ + c_-\boldsymbol{\nabla}\mu_-), \tag{5.2}$$

where $p' = p - (c_+ + c_-)$, now incorporates the osmotic pressure.

5.1 Limiting current

In an electrochemical system like the sketch Fig. 5.2 represents, we can describe the current-voltage relationship in the system in the absence of advection. In the rest of the thesis, current and current density will be used interchangeably.

The system in Fig. 5.2, consists of a binary electrolyte between two electrodes ($\partial\Omega_1$ & $\partial\Omega_2$), and with no surface charge on either side ($\partial\Omega_3$ & $\partial\Omega_4$). Because of the symmetry, variations happens only the x-direction, which reduces the equations to one dimension. The inlet of the system, $\partial\Omega_1$, acts as a reservoir of the ionic species and as an electrode held at zero volt,

$$c_\pm(0) = c_0, \quad \phi(0) = 0. \tag{5.3}$$

The electrode at boundary $\partial\Omega_2$, can be thought of as a membrane, impenetrable to one species of ions, hence the current of that species, in this case the anions, is zero, $J_{x,-} = 0$. The only current is thus that of the cations $J_{x,+} = R$, where R is a reaction rate which we account for later. The electrode is held at a fixed negative voltage and this concludes the boundary conditions,

$$\phi(L) = -V_0. \tag{5.4}$$

In the absence of advection, the current is a function of the electrochemical potential, and using the fixed concentration at the inlet we can describe the anions as a function of the potential,

$$c_-(x) = c_0 \exp\left(\frac{\phi(x)}{V_T}\right). \tag{5.5}$$

A widely used assumption is that of electro neutrality, because it is a more favourable configuration in terms of energy. This can be seen, from the Poisson-equation, where the dimensions has been collected in the Debye-length,

$$\nabla^2 \tilde{\phi} = \frac{1}{2\lambda_D^2}\left[\tilde{c}_+ - \tilde{c}_-\right]. \tag{5.6}$$

Since the Debye-length has typical values $\lambda_D \approx 10\,\mathrm{nm}$, even a small break of charge neutrality will force the potential distribution to act to stabilize this difference.

We will at first assume that the system will try to stay electrically neutral in all of the system hence $c_+ = c_-$, which allow us to write the equation for the cation current, by insertion of equation Eq. (5.5) into Eq. (2.20) and ignoring advection,

$$J_+ = -D_+ c_0 \partial_x \left(\exp\left[-\frac{\phi(x)}{V_T}\right]\right) - \frac{D_+ c_0}{V_T}\exp\left[-\frac{\phi(x)}{V_T}\right]\partial_x \phi(x), \tag{5.7a}$$

$$J_+ = -2D_+ c_0 \partial_x \exp\left[-\frac{\phi(x)}{V_T}\right]. \tag{5.7b}$$

Integrating this expression subjected to the boundary condition for the potential at the inlet, Eq. (5.3), we find an expression for the relationship between the current and the electric potential,

$$\phi(x) = V_T \log\left(1 - \frac{J_+}{2D_+ c_0}x\right). \tag{5.8}$$

Since we are interested in the maximum current, as a function of the applied voltage we employ the boundary condition, $\phi(L) = -V_0$, which yields,

$$V_0 = -V_T \log\left(1 - \frac{J_+}{J_{\lim}}\right), \tag{5.9}$$

where we have introduced the diffusion limited current $J_{\lim} = \dfrac{2D_+ c_0}{L}$. This term will also be presented as just the limiting current.

5.2   Electrode

Electrode kinetics is a complicated field of study, that we will not engage in here. A phenomenological model for the electrode kinetics exist, known as the Butler–Volmer equation. The full equation incorporate many properties of the specific electrode reaction,

but we will work in a limit of the Butler-Volmer equation, where we assume negligible overpotentials. In that case we can write a simple expression for the electrode reaction rate,

$$R = k_0 \left(\frac{c_+}{c_0} - 1 \right), \tag{5.10}$$

where k_0 is a reaction constant, having the dimensions of a current density $[k_0] = \mathrm{m}^{-2}\,\mathrm{s}^{-1}$. At cation concentrations, at the interface larger than the bulk concentration, the reaction occurs in forward direction and opposite for lower concentrations. This simple model is inspired by the work of Bazant [2].

Having an expression for the current at the electrode boundary, allows us to make a correction to Eq. (5.9). In this expression electroneutrality is assumed in all of the system, but we know that this is not upheld in the Debye-layer. If we introduce a new concentration c_+^*, defined as the concentration at the electrode boundary, we will assume that the concentration immediately outside the Debye-layer is related to the electrode concentration through a Boltzmann relation, with some potential drop across this layer,

$$c_+^* = c_+ \exp \left[-\frac{\Delta V}{V_T} \right], \tag{5.11}$$

where ΔV is this potential drop across the Debye-layer. We assume that the Debye-layer is very thin compared to the length of the system, so the potential drop happens at the same position $x = L$. Employing now the expression for the the electrode current defined by the reaction rate R, in Eq. (5.10) we write,

$$J_+ = k_0 \left(\frac{c_+^*}{c_0} - 1 \right) = k_0 \left(\frac{c_+}{c_0} \exp \left[-\frac{\Delta V}{V_T} \right] - 1 \right). \tag{5.12}$$

From this expression we can determine the potential drop across the Debye-layer,

$$\Delta V = -V_T \log \left[\frac{c_0}{c_+} \left(\frac{J_+}{k_0} + 1 \right) \right] = -V_T \log \left[\frac{1}{1 - J_+/J_{\mathrm{lim}}} \left(\frac{J_+}{k_0} + 1 \right) \right]. \tag{5.13}$$

In the last equality we have combined Eq. (5.5) with Eq. (5.8), to write the cation concentration in terms of the current. The total potential drop in the system is now determined as the sum of the drops in the bulk electroneutral region and the Debye-layer.

$$-V_0 = \phi_{\mathrm{bulk}} + \Delta V = V_T \log \left[1 - \frac{J_+}{J_{\mathrm{lim}}} \right] - V_T \log \left[\frac{1}{1 - J_+/J_{\mathrm{lim}}} \left(\frac{J_+}{k_0} + 1 \right) \right], \tag{5.14}$$

Which reduces to,

$$-V_0 = V_T \log \left[\frac{\left(1 - J_+/J_{\mathrm{lim}} \right)^2}{\left(1 + J_+/k_0 \right)} \right]. \tag{5.15}$$

5.3   Numerical setup

We present here the numerical setup used to obtain the results shown in the nest chapter. The model system is sketched in Fig. 5.3, and it shows the model representation of a dendrite. Even though the dendrite morphology is much more complicated, this is thought of as representing an early state of the dendrite. The Gaussian shape has been used because of the smooth varation, which ease the numerical calculations. The function describing the dendrite is,

$$D(y) = L - h \exp\left[-\frac{1}{2}\left(\frac{1/2 - y/H}{w}\right)^2\right]. \tag{5.16}$$

This allow us to change the shape of the electrode, by varying w. The height of the dendrite h, was held fixed in this study, to be able to compare the results, and the values are shown in Table 5.1.

   The boundaries $\partial\Omega_3$ and $\partial\Omega_4$ in Fig. 5.3 was modelled in a way as to extend the system periodically at both boundaries. This was done because the early experiments suggested that with boundary conditions representing walls was confining the advection rolls, and we wanted to model a bulk system, and not a microchannel.

   Furthermore, all modelling is in steady state, since incorporating the various growth mechanisms and modelling the time evolutions of the fields is beyond the scope of this work.
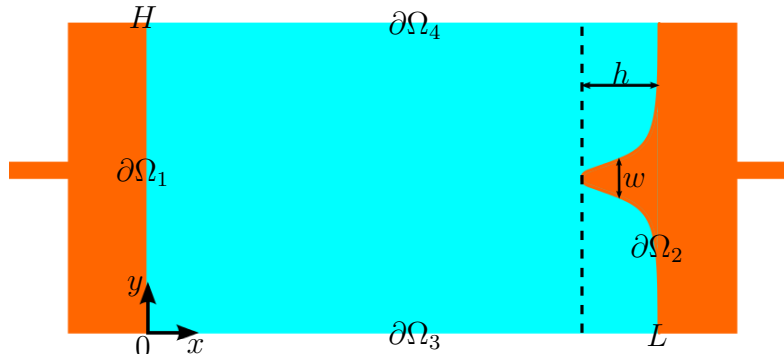

Figure 5.3: Sketch of geometry with Gaussian dendrite electrode

5.3.1   Stokes equation

Since we want to implement the dynamics of the electrolyte into our model, which is described by the Navier–Stokes equation introduced in Section 2.1. With the parameters outlined in Table 5.1, and assuming velocities $v \leq 1\,\mathrm{mm\,s^{-1}}$ the Reynolds-number will not exceed 10^{-2}. We will therefore assume the limit of low Reynolds-numbers valid, and reduce equation Eq. (2.6b) to the linear Stokes equation,

$$\boldsymbol{\nabla}\cdot\boldsymbol{\sigma} + \boldsymbol{f} = 0, \tag{5.17}$$

Table 5.1: Table of the range of values used in the dendrite model system. In the value of the permittivity ϵ_0 denotes the permittivity of vacuum.

Description	Symbol	Value
Length of system	L	[2-20] µm
Height of system	H	[2-10] µm
Bulk concentration of ions	c_0	[0.01-100] mM
Temperature	T	300 K
Diffusivity of ions	$D_\pm$	$2 \times 10^{-9}\,\mathrm{m^2\,s^{-1}}$
Permittivity of electrolytic solution	ϵ	$78\epsilon_0$
Density of solution	ρ	$1 \times 10^{-3}\,\mathrm{kg\,m^{-3}}$
Viscosity of solution	η	$1.002 \times 10^{-3}\,\mathrm{Pa\,s}$
Amplitude of dendrite	h	1 µm
Width of dendrite	w	[0.5-0.02]
Reaction constant	k_0	$D_+ c_0/L$

where $\boldsymbol{\sigma}$ is the Cauchy stress-tensor for an incompressible fluid with components,

$$\sigma_{ij} = -p_i\delta_{ij} + \eta(\partial_j v_i + \partial_i v_j), \tag{5.18}$$

and $\boldsymbol{f}$ is the body-force-density described by the electro-chemical potential,

$$\boldsymbol{f} = -(c_+\boldsymbol{\nabla}\mu_+ + c_-\boldsymbol{\nabla}\mu_-). \tag{5.19}$$

We have 2 dependent variables in the equation, the velocities, v_i, where i denotes the y- and x-direction, and we therefore have two weak Stokes-equations,

$$\int_{\partial\Omega} \hat{v}_{i,m}\boldsymbol{n}\cdot\boldsymbol{\sigma}_i\mathrm{d}A + \int_{\Omega}[-\boldsymbol{\nabla}\hat{v}_{i,m}\cdot\boldsymbol{\sigma}_i + \hat{v}_{i,m}f_i\mathrm{d}V = 0. \tag{5.20}$$

Here the weak boundary expression is implemented on boundary $\partial\Omega_1$ along with a constraint

$$\partial_x v_x = 0, \quad v_y = 0, \quad \boldsymbol{r} \in \{\partial\Omega_1\}, \tag{5.21}$$

coupling the velocity field to the weak contribution through $\boldsymbol{\sigma}$ and constrains the inflow to be in the x-direction only, with no variations along the inlet. At the electrode, $\partial\Omega_2$ we employ a no slip boundary condition for the velocity fields,

$$v_x = 0, \quad v_y = 0, \quad \boldsymbol{r} \in \{\partial\Omega_2\}. \tag{5.22}$$

On the sides of the system, $\partial\Omega_3$ and $\partial\Omega_4$ we constrain the y component of the velocity,

$$v_y = 0, \quad \boldsymbol{r} \in \{\partial\Omega_3, \partial\Omega_4\}, \tag{5.23}$$

which introduces the periodic boundary condition on each side of the domain, where the y component of the velocity cancels due to symmetry.

5.3.2 Continuity equation

The continuity equation, introduced in Eq. (2.3), is used as the equation for the pressure field in the system. We multiply the continuity equation by the test function for the pressure and integrate over the domain,

$$\int_{\Omega} \hat{p}_m \boldsymbol{\nabla} \cdot \boldsymbol{v} \mathrm{d}V = 0. \tag{5.24}$$

Since we are already dealing with derivatives of $\boldsymbol{v}$ in the Stokes equation, no simplification is obtained by splitting the integral in a boundary and a bulk part[8]. Due to the electrode at boundary, $\partial\Omega_2$, the only constraint we impose on the pressure is at the inlet, $\partial\Omega_1$,

$$p = 0, \quad \boldsymbol{r} \in \{\partial\Omega_1\}, \tag{5.25}$$

hence no external pressure difference is applied.

5.3.3 Nernst–Planck equation

The implementation of the Nernst–Planck equation is altered slightly compared to Section 4.3.2. With the change of variable $c_\pm \to \log \tilde{c}_\pm$, the weak form reads,

$$\int_{\partial\Omega} \log \hat{c}_{\pm,m} \boldsymbol{n} \cdot \boldsymbol{J}_\pm \mathrm{d}A + \int_{\Omega} (-\boldsymbol{\nabla} \log \hat{c}_{\pm,m} \cdot \boldsymbol{J}_\pm) \mathrm{d}V = 0. \tag{5.26}$$

Because of the symmetry in the system we have no net flux through $\partial\Omega_3$ and $\partial\Omega_4$, so the no flux boundary condition applies,

$$\boldsymbol{n} \cdot \boldsymbol{J}_\pm = 0, \quad \boldsymbol{r} \in \{\partial\Omega_3, \partial\Omega_4\} \tag{5.27}$$

On the electrode boundary, $\partial\Omega_2$, a weak contribution is applied corresponding to the electrode reaction rate Eq. (5.10), so that the boundary current densities reads,

$$\boldsymbol{n} \cdot \boldsymbol{J}_+ = gk_0 \left(\frac{c_+}{c_0} - 1 \right), \quad \boldsymbol{n} \cdot \boldsymbol{J}_- = 0, \quad \boldsymbol{r} \in \{\partial\Omega_2\}. \tag{5.28}$$

Here g has been introduced, representing a conductivity of the electrode, and this is one of the parameters we will consider in the study. The inlet, $\partial\Omega_1$, acts as a reservoir for the system so the concentration is constraint here,

$$c_\pm = c_0, \quad \boldsymbol{r} \in \{\partial\Omega_1\}. \tag{5.29}$$

5.3.4 Poisson equation

We implement the Poisson equation in the bulk as in Section 4.3.1,

$$\int_{\partial\Omega} \hat{\phi}_m \boldsymbol{n} \cdot (-\epsilon \boldsymbol{\nabla} \phi) \mathrm{d}A + \int_{\Omega} \big[- \boldsymbol{\nabla}\hat{\phi}_m \cdot (-\epsilon \boldsymbol{\nabla} \phi) - \hat{\phi}_m \rho_{\mathrm{el}} \big] \mathrm{d}V = 0, \qquad (5.30)$$

but with the periodicity in boundaries $\partial\Omega_3$ and $\partial\Omega_4$ no surface charge is present and the weak boundary contribution is,

$$\boldsymbol{n} \cdot (-\epsilon \boldsymbol{\nabla} \phi) = 0, \; \boldsymbol{r} \in \{\partial\Omega_3, \partial\Omega_4\}. \qquad (5.31)$$

Instead we apply a potential difference between the electrode, $\partial\Omega_1$, and the inlet, $\partial\Omega_2$, and this is implemented as a constraint on the potential,

$$\phi = 0, \; \boldsymbol{r} \in \partial\Omega_1 \quad \phi = -V_0, \; \boldsymbol{r} \in \partial\Omega_2. \qquad (5.32)$$

5.3.5 Mesh convergence analysis

As described in Section 3.2 it is important in numerical studies to make sure that the mesh on the computational domain is good enough, to avoid numerical artefacts in the solution. Especially the boundaries tend to be a problem because of the great variation in the fields in the vicinity of a surface. In this study, we pay close attention to the electrode boundary, because changes in the fields here happens typically in Debye-lengths, which for the parameters shown in Table 5.1 takes the values $\lambda_{\mathrm{D}} = [0.5\text{-}100]$ nm.

There are different mesh types to choose between when meshing a boundary. One option is to use the triangular mesh elements used in the bulk and refine the size, another is to create rectangular boundary mesh elements. The latter was chosen for this problem because of the possibility to make very thin stacks of elements. This is particularly good here, since the strongest field gradients are in the normal direction.

The mesh element size, $d_{\mathrm{mesh}}^{\mathrm{blk}}$, of the elements in the bulk, was chosen to $d_{\mathrm{mesh}}^{\mathrm{blk}} = 0.5\,\mu\mathrm{m}$ and in the boundary layer the size of the smallest element was chosen to $d_{\mathrm{mesh}}^{\mathrm{blk}} = 1\,\mathrm{nm}$ for a Debye-layer thickness of $\lambda_{\mathrm{D}} = 10\,\mathrm{nm}$. The normal approach in mesh convergence analysis is to sweep over the bulk, or the boundary layer, mesh size. But because of the way the dendrite boundary was constructed, we chose the maximum element growth rate α_{mesh} as the parameter to refine the mesh in this study. This controls at what rate the mesh size grows from the smallest to the biggest. Fig. 5.4 shows the mesh convergence parameter C as introduced in Eq. (3.11), calculated for different α_{mesh} in the interval $\alpha_{\mathrm{mesh}} = [2\,\%\text{-}100\,\%]$ and the corresponding number of degrees of freedom, DoF, was used for the plot. The reference solution g_{ref} was calculated for $\alpha_{\mathrm{mesh}} = 1\,\%$ corresponding to 1×10^7 DoF.
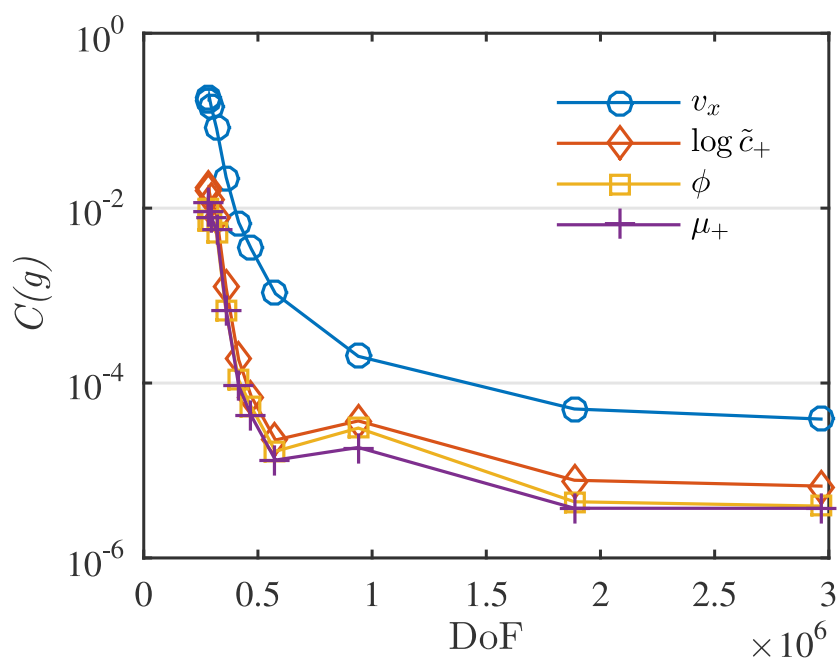
Figure 5.4: Mesh convergence analysis performed on the field variables v_x, ϕ, $\log \tilde{c}_+$ and μ_+. The convergence parameter $C(g)$ was calculated as in Eq. (3.11), with the reference solution g_{ref} calculated with growth rate $\alpha_{\text{mesh}} = 1\%$. The convergence parameter is plotted as a function of the number of degrees of freedom in the system, DoF. We chose $\alpha = 1.1$, corresponding to 0.5×10^6 DoF, and relative mesh convergence parameter $C < 10^{-3}$, for the rest of the study.

Chapter 6

Results

As presented in Section 5.1, the current in an electrochemical system, as a function of the applied voltage will converge to the limiting current J_{lim} in the absence of advection contributions. We have produced current-voltage characteristics for different system-parameters and compared the results from the models with and without advection. Here the models without advection involves only the Poisson-Nernst-Planck equations.

The current distribution on the dendrite and in the rest of the system has also been investigated, in the presence of advection rolls.

6.1 Overlimiting current

In the conducted studies we saw an effect of advection on the current densities for large V_0, except in some low concentration cases. We have investigated different values of the electrode conductivity g, dendrite width w, bulk concentration c_0 and system height H, to see what parameters contribute to the advection overlimiting current. In Fig. 6.2a the width of the electrode has been varied from a sharp peak dendrite $w = 0.02$ to an almost flat dendrite $w = 0.5$, as shown in Fig. 6.1.

Figure 6.1: Example of two different dendrite widths used in the numerical study.

For all of the width we see that the advection rolls had an effect on the current, but that the voltage at which the effect begins, deviate. For the sharp protrusion $w = 0.02$ the effect is visible at $\tilde{V}_0 = 13$ and for the flat protrusion $w = 0.5$ the effect kicks in at $\tilde{V}_0 = 20$. It is unclear what this difference stems from, but may be because of a larger tangential electric field component, which we discuss in the next section. The limiting current for the different width vary slightly, but this might stem from the definition of the limiting current $J_{\text{lim}} = \dfrac{2D_+ c_0}{L}$, since it is dependent on system length. The dendrite has a fixed amplitude $h = 1\,\mu\text{m}$, but the wide dendrite occupy more of the space near this height than the narrow one. This results in a larger limiting current
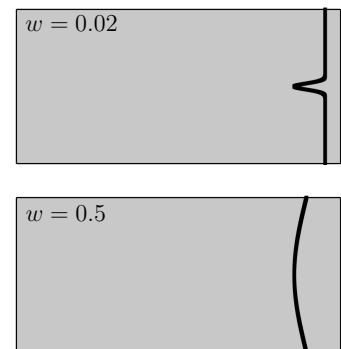
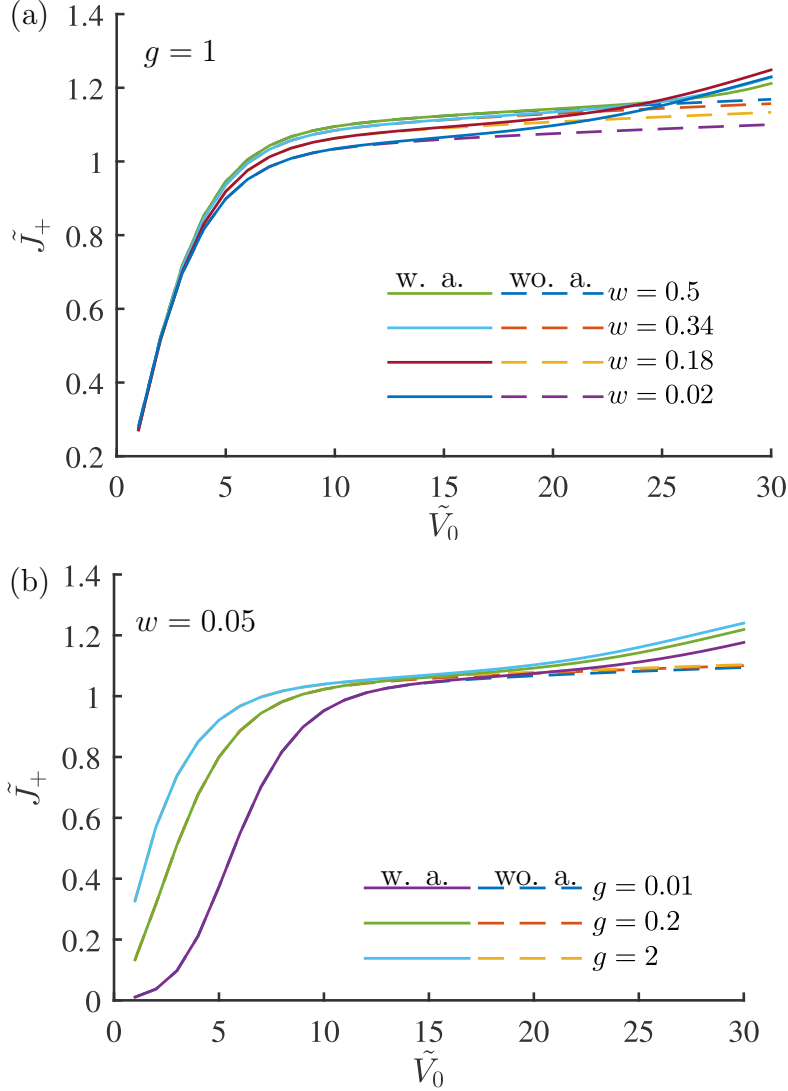for the flat dendrite than for the narrow, which agrees with what we see.

Figure 6.2: Both results were obtained with the system parameters $H = 5\,\mu m$, $L = 10\,\mu m$, $c_0 = 1\,mM$. The full lines are results with advection (w. a.) and the dashed lines without advection (wo. a.). The current is normalized by the limiting current $\tilde{J}_+ = J_+/J_{\text{lim}}$ and the voltage is normalized by the thermal voltage $\tilde{V}_0 = V_0/V_T$. (a) IV-characteristic for varying electrode width w with conductivity $g = 1$. (b) IV-characteristic for varying conductivities g, with electrode width $w = 0.05$.

In Fig. 6.2b the electrode conductivity has been varied from a bad conductor $g = 0.01$ to a good conductor $g = 2$. As for the different dendrite widths, we see an overlimiting current from advection rolls. The conductivity does not play an important role in this

aspect. The variations in the current densities at low voltage can be explained, since it takes a large voltage to drive a current, if the conductivity of the electrode is low. This is also in agreement with the correction to the model of the limiting current Eq. (5.15), where the variations in conductivity can be compared to varying the reaction constant k_0, and during the studies we could confirm that the corrected IV-expression was in good agreement with the numerical results.

We have investigated if the bulk concentration influence the advection contribution to the current density. A wide range of concentrations has been examined, and the resulting IV-characteristic is shown in Fig. 6.3b. For low concentrations, the results with and without advection coincide (blue line), hence bulk advection. in this concentration regime, did not contribute to the current. The range of concentrations between $c_0 = 0.01\,\text{mM}$ and $c_0 = 1\,\text{mM}$ was investigated further to see where the bulk advection begins to play role, and we found that for $c_0 > 0.02\,\text{mM}$ the effect of advection could be seen.

In the low concentration regime, we thus see an overlimiting current that stems from something else. Since the Debye-length, scales inversely with the concentration squared we have Debye-lengths $\lambda_\text{D} \simeq 100\text{nm}$ in this regime. In the derivation of the limiting current, we assume that the system will try to stay electroneautral, but this condition is less strict for longer Debye-lengths, which can be seen in from the version of the Poisson-equation presented in Eq. (5.6). In this case the electroneutrality condition is less strict and the system might respond to the driving force by breaking neutrality resulting in an overlimiting current.

It is very clear from Fig. 6.3a that the physical dimensions of the system have a great impact on the advection contribution to the current density. The range of studied voltages was expanded $V_0 = [1\text{-}50]V_T$ when this effect was noticed. For the narrow system, $H = 2\,\mu\text{m}$, the current does not exceed the limiting current, even for large voltages. We noticed that the maximum velocity of the fluid stays low, compared to the larger systems. This might have an influence on the, lack of overlimiting current in this system. When we increased the height no limit on the current was found, in the studied range of voltages.

6.2 Advection rolls near dendrite tip

As presented above the presence of advection rolls in the system contribute to the current in such a way as to allow an overlimiting current. An example of the advection rolls near the dendrite tip is shown in Fig. 6.4, showing that the largest velocities occur in the vicinity of the dendrite tip. This behaviour of the fluid was apparent for all of the investigated parameter combinations. The driving of the rolls stems from a tangential component of the electric field exerting a body force on the charge density in the Debye-layer. Normally in problems involving electro osmotic flows, an electro osmotic velocity is defined as,

$$v_\text{eo} = \frac{\epsilon_w V_0}{\eta} E_\parallel \tag{6.1}$$

where $E_\parallel$ in this definition is the electric field component tangential to the electrode. We were not able to obtain the electric field component in the tangential direction, but to
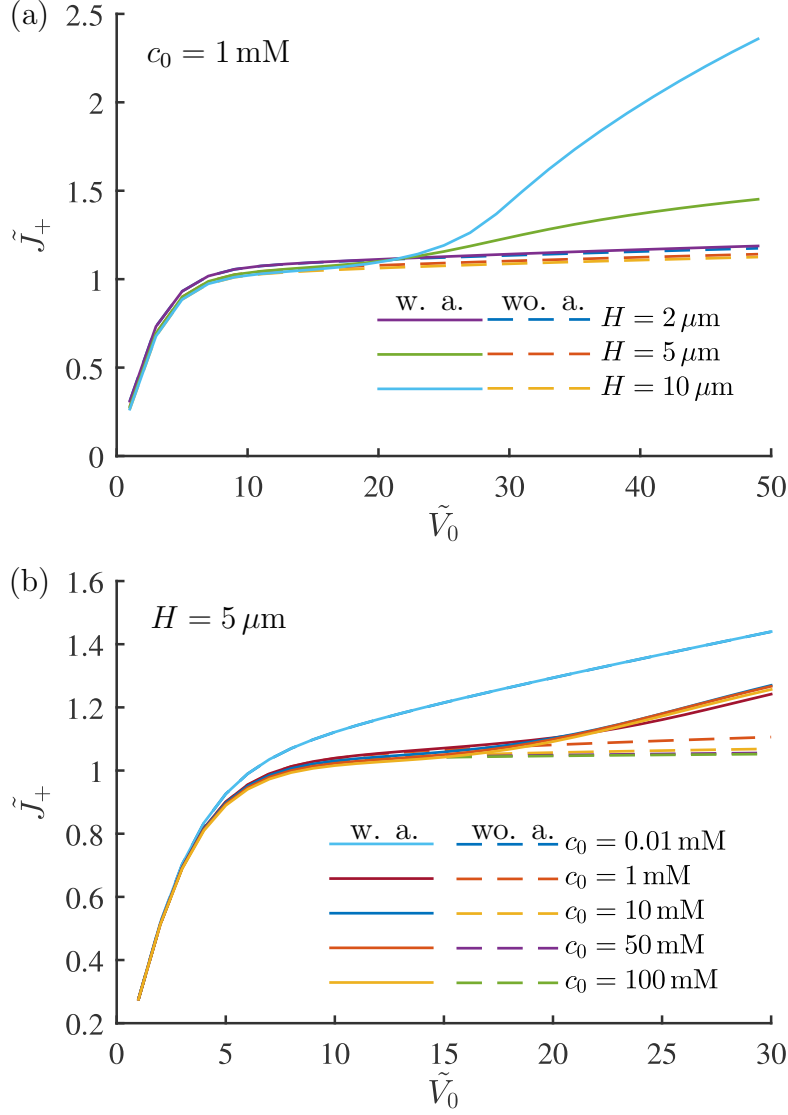
Figure 6.3: Both results were obtained with the system parameters $L = 10\,\mu\mathrm{m}$, $g = 1$ and $w = 0.05$. The full lines are results with advection (w. a.) and the dashed lines without advection (wo. a.). The current is normalized by the limiting current $\tilde{J}_+ = J_+/J_{\lim}$ and the voltage is normalized by the thermal voltage $\tilde{V}_0 = V_0/V_T$. (a) IV-characteristic for varying system height H with bulk concentration $c_0 = 1\,\mathrm{mM}$. Note the larger range of V_0. (b) IV-characteristic for varying bulk concentration c_0, with system height $H = 5\,\mathrm{mM}$

get an idea of the field required, we calculated this using the velocity magnitude for the different applied voltages. We found that for a system height $H = 10\,\mu\mathrm{m}$ and an applied voltage $V_0 = 20V_T$, the magnitude of the velocity was $|v| = 5\,\mathrm{mm\,s^{-1}}$, as seen in Fig. 6.4a.
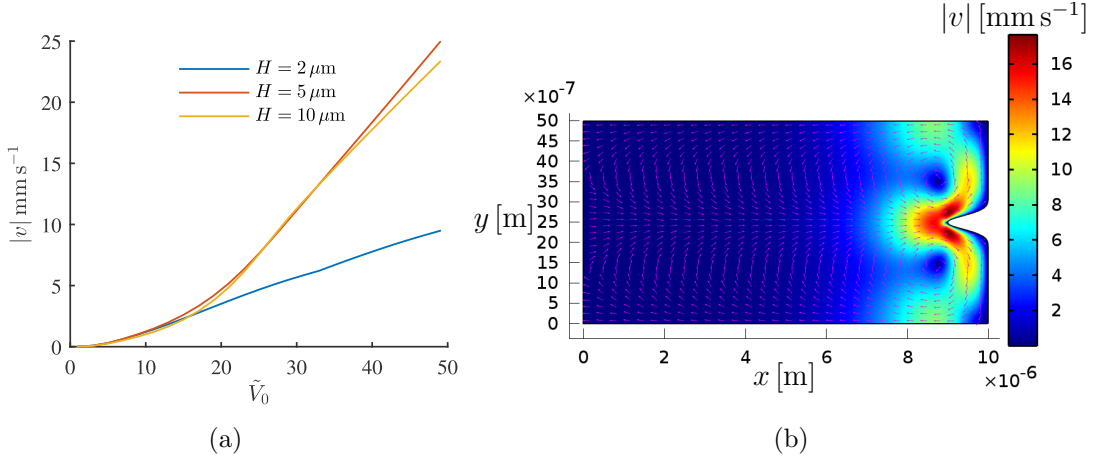
Figure 6.4: (a) Plot of the velocity magnitude $|v|$ against the normalized applied voltage $\tilde{V}_0$ for different system heights H. (b) Contour of the magnitude of the velocity $|v|$ (color plot). The arrows in magenta indicates the velocity field components v_x and v_y. The figure was obtained with the system parameters $\tilde{V}_0 = 40$, $c_0 = 1\text{mM}$, $g = 1$ and $w = 0.05$.

This results in an required tangential electric field component $E_\parallel = 0.012\,\text{V}\mu\text{m}^{-1}$. The normal electric field in the Debye-layer, from the tip of the dendrite was for the same parameters calculated to $E_\perp = 34\,\text{V}\,\mu\text{m}^{-1}$, hence only a small fraction of the this field is needed to drive the rolls. Due to time limitations, further investigations did not make it into the report.

One important contribution that we encountered was distribution of the current on the electrode, which is shown in Fig. 6.5. The boundary current distribution is shown for two values of the applied voltage, $V_0 = 20\,V_T$, which compared to Fig. 6.3 is in the voltage regime without advection effects and $V_0 = 40\,V_T$, which is in the regime with advection effects. In the leftmost graph, Fig. 6.5a, the distrubution of current along the electrode is the same for both of the applied voltages, and with and without advection. For $H = 5\,\mu\text{m}$, in Fig. 6.5b, we start to see an effect of advection at the large voltage, where the current distribution increases near the dendrite tip. The same is the case in Fig. 6.5c, where for $H = 10\,\mu\text{m}$ we see a peak current density of close to $20\,J_{\text{lim}}$. If this trend can be verified in larger systems, and nonsymmetrical setups, it may have an impact on the growth of the dendrites, since this is conditional on the current distribution.

The last subject under investigation is the current of the cations in the rest of the system as well. In Fig. 6.6 a contour of the logarithm to the normalized current density $\log\left[\tilde{J}_+\right]$ is shown, in the presence of advection rolls, and the arrows shown in magenta are the x- and y-components of the current. We chose the logarithm, to be able to see the differences in the field. In Fig. 6.7 the same system is shown but in the absence of advection rolls. In the absence of advection the only differences occur near the tip and this is in agreement with Fig. 6.5b, showing the peak at the dendrite tip and the valleys at the dendrite side. In the presence of advection it seems like the rolls confine the current
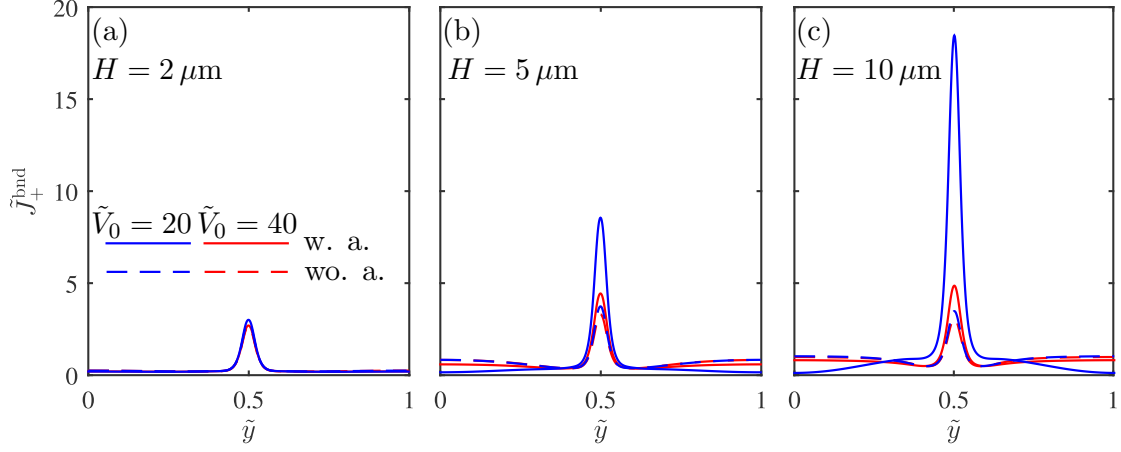
Figure 6.5: Current density evaluated at the electrode for the system heights (a) $H = 2\,\mu$m, (b) $H = 5\,\mu$m and (c) $H = 10\,\mu$m. The current density is normalized by the limiting current and the y-axis is normalized by the system height. The results were obtained with the system parameters $c_0 = 1$mM, $g = 1$, $w = 0.05$. Solid line denotes results obtained with advection (w. a.), dashed line without advection (wo. a.). The results shown in blue were obtained with an applied voltage $\tilde{V}_0 = 20$, the results shown in red with an applied voltage $\tilde{V}_0 = 40$.

to the middle of the system, creating a passage for the current. This effect was even more visible in larger system. We suspect that it is mostly due to the symmetry in the system, because what the dendrite sees on either side is a mirror image of the system itself, and that it has less to do with each roll itself. This would be interesting to pursue further for different geometries and larger systems.
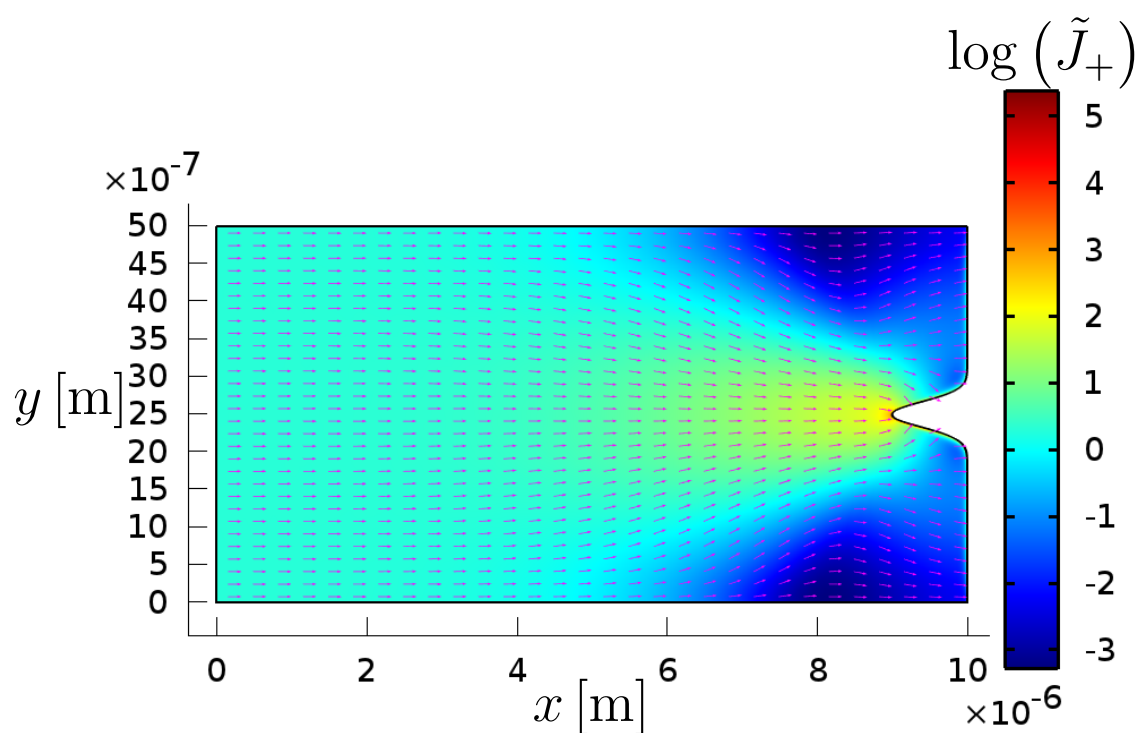
Figure 6.6: Contour showing the logarithm to the normalized cation current density $\log\left(\tilde{J}_+\right)$(color plot) and the current density components (arrow plot), in the presence of advection. The figure was obtained with the system parameters $\tilde{V}_0 = 40$, $c_0 = 1\text{mM}$, $g = 1$ and $w = 0.05$.

Figure 6.7: Contour showing the logarithm to the normalized cation current density $\log\left(\tilde{J}_+\right)$ (color plot) and the current density components (arrow plot), in the absence of advection. The figure was obtained with the system parameters $\tilde{V}_0 = 40$, $c_0 = 1\text{mM}$, $g = 1$ and $w = 0.05$.
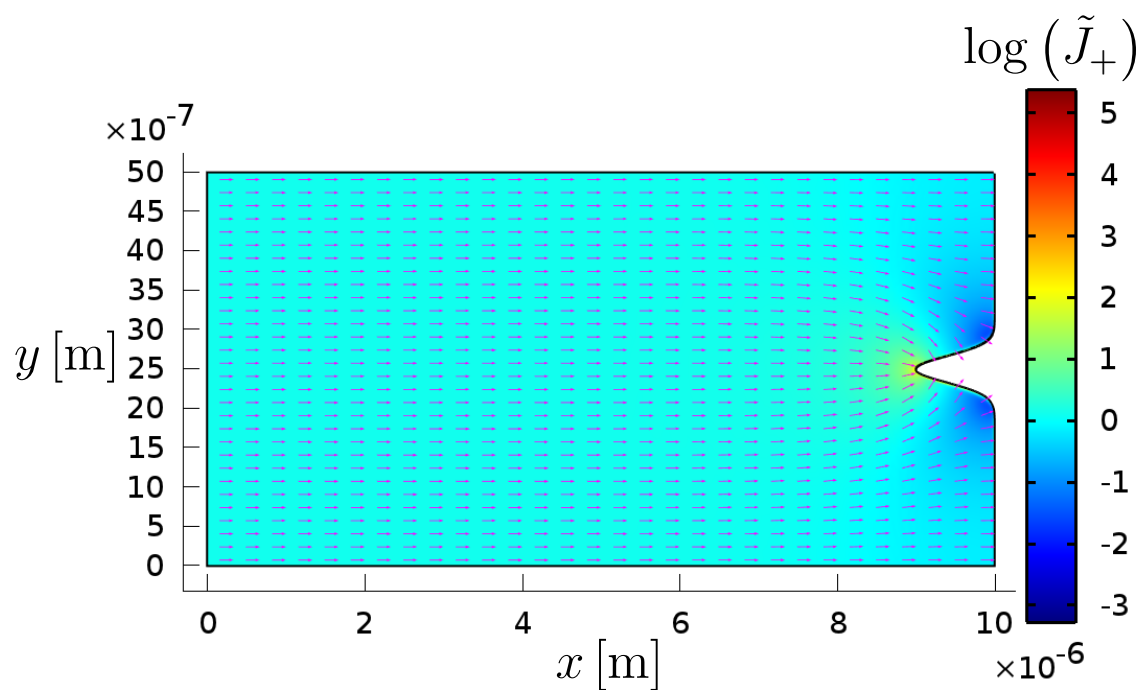
Chapter 7

Conclusion and outlook

We present here a brief outlook and discussion, of what further investigations could be pursued, as well as the final concluding remarks on the thesis.

7.1 Outlook

The results presented in the previous chapter were obtained from simulations of a small system, compared to the work of other authors. Experimentals setups with the dimensions $H = 1\,\mathrm{mm}$ and $L = 25\,\mathrm{mm}$ has been carried out in the study of the convection rolls around dendrites [7], and it would be interesting to carry out numerical simulations on such a system, since the exiting theory fails in predicting the velocity of the rolls[9]. This was however not possible since the increased size, was to heavy in computational time, if the resolution of the problem was to be kept. We did carry out some simulations on larger systems ($H = 45\,\mathrm{\mu m}$ $L = 100\,\mathrm{\mu m}$) inspired by experiments on growth of dendrites [5], but already for this size we had trouble with the mesh convergence. Further investigations into larger systems would require that this problem was dealt with in some way, maybe by a coupling between a model of the boundary layer and a model of the bulk system.

The expression used for the reaction kinetics at the electrode is a simple limit of the Butler-Volmer equation. In future studies it could be relevant to extend the expression, by incorporating more physics, either to verify the approximation used or to investigate were it breaks down.

The mentioned experimental setup used by Huth. et. al. [7], measured velocities with a magnitude of $|v| = 10\,\mathrm{\mu m\,s^{-1}}$, for a system with the mentioned dimensions $H = 1\,\mathrm{mm}$ and $L = 25\,\mathrm{mm}$, a dendrite width of $w \approx 0.2\,\mathrm{mm}$ and a bulk concentration $c_0 = 10^{-2}\,\mathrm{mM}$ and it was driven by a constant electric current density of $4\mathrm{mA\,cm^{-1}}$. In units of the limiting current for that setup the current density is $\tilde{J}_{\mathrm{exp}} = 10^5$. This seemed a good parameter to compare the systems on but we did not reach currents of this magnitude. The maximum velocity for the same concentration in our numerical study was observed to $|v| = 100\,\mathrm{\mu m\,s^{-1}}$, already at $\tilde{J} = 1.4$. Everything indicated that velocities rose with the current, which suggest that other parameters, that we have not investigated, play a role on the velocity of the advection rolls.

7.2   Conclusion

We have in this thesis studied electrokinetics with advection near an ideal model of a dendrite. We have explained the behaviour of an electrolytic solution near a charged surface by introducing the idea of a Debye screening layer. An analytical solution was found to the Poisson–Botzmann equation in a simple setup, and it was compared to a numerical model.

A simple model of the diffusion limited current density was presented, and corrected to take into account the breakdown of charge neutrality in the Debye-layer. We have presented the implementation of the Poisson-Nernst-Planck-Stokes problem in COMSOL multiphysics and carried out numerical experiments on a dendritic metal electrode.

We saw that advection rolls contributed to an overlimiting current, and that the physical dimensions of the model system played a role in the amount of overlimiting current. The advection rolls were also found to increase the amount of current into the tip of the dendrite, and that this effect scaled with the height of the system. The cation current distribution in the system was investigated, and we found that the advection rolls created a region from the reservoir to the tip of the dendrite with a large current density.

Bibliography

[1] Henrik Bruus, *Theoretical Microfluidics*, Oxford Univeristy Press (Oxford 2008).

[2] Theory of Chemical Kinetics and Charge Transfer based on Nonequilibrium Thermodynamics,
Martin Z. Bazant,
Accounts of Chemical Research **46** 5, 1144-1160, (2013).

[3] *Numerical study of thermoviscous effects in ultrasound-induced acoustic streaming in microchannels*,
Henrik Bruus, Peter Barkholt Muller,
Physical Review E **90**, 043016, 1-12, (2014).

[4] *Concentration polarization, surface currents, and bulk advection in a microchannel*,
Henrik Bruus, Christoffer P. Nielsen,
Physical Review E **90**, 043020, 1-14, (2014).

[5] *Growth of electrolytic copper dendrites. I: Current transients and optical observations*
O. Devos, C. Gabrielli, L. Beitone, C. Mace, E. Ostermann and H. Perrot,
Journal of Electroanalytical Chemistry **606**, 75-85, (2007).

[6] *Theory and Experimental Evidence of Electroconvection around Electrochemical Deposits*,
V. Fleury, J.-N. Chazalviel and M Rosso,
Physical Review Letters **68**, 2492-2495, (1992).

[7] *Role of convection in thin-layer electrodeposition*
John M. Huth, Harry L. Swinney and William D. McCormick,
Physical Review E **51**, 3444-3458, (1995).

[8] *Theory and simulation of electrokinetics in micro- and nanochannels*,
Christoffer P. Nielsen, DTU Msc. Thesis (2012)
Source URL: `http://www.staff.dtu.dk/bruus/Researchgroup/TMFthesesMSc`

[9] *Electrodeposition from a binary electrolyte: new developments and applications*
Michel Rosso,
Electrochimica Acta **53**, 250-256, (2007).

[10] *Pattern morphologies in zinc electrodeposition*,
Pedro Pablo Trigueros, Josep Claret, Francesc Mas, Francesc Sagués.
J. Electroanal. Chem. **312**, 219-235, (1991).

[11] Source URL (retrieved on 05/18/2015 - 09:32):
`http://batteryuniversity.com/learn/article/battery_statistics`

[12] *Trace Degradation Analysis of Lithium-Ion Battery Components*,
Paul Voelker, Thermo Fisher Scientific, Sunnyvale, Calif.
Source URL (retrieved on 05/18/2015 - 10:32): `http://www.rdmag.com/articles/`
`2014/04/trace-degradation-analysis-lithium-ionbattery-components`

[13] *COMSOL Multiphysics Users Guide*,
Source URL (retrieved on 06/08/2015 - 16:21):
`http://nf.nci.org.au/facilities/software/COMSOL/4.3/doc/pdf/mph/`
`COMSOLMultiphysicsUsersGuide.pdf`